

# **Extended MHD Modeling of Tearing-Driven Magnetic Relaxation**

J. P. Sauppe<sup>1</sup> and C. R. Sovinec

**University of Wisconsin-Madison  
Center for Plasma Theory and Computation  
Report UW-CPTC 16-6**

November 17, 2016

This article has been submitted to the Physics of Plasmas, <http://aip.scitation.org/toc/php/current>, for publication in the special issue featuring invited presentations from the 2016 Annual Meeting of the APS Division of Plasma Physics.

## NOTICE

This report was prepared as an account of work sponsored by an agency of the United States Government. Neither the United States Government, nor any of their employees, makes any warranty, express or implied, or assumes any legal liability for the accuracy, completeness, or usefulness of any information, apparatus, product, or process disclosed, or represents that its use would not infringe privately owned rights. Reference herein to any specific commercial product, process, or service by trade name, trademark, manufacturer, or otherwise does not necessarily constitute or imply its endorsement, recommendation, or favoring by the United States Government or any agency thereof. The views and opinions of authors expressed herein do not necessarily state or reflect those of the United States Government or any agency thereof.

---

<sup>1</sup>Presently at Los Alamos National Laboratory, Los Alamos, New Mexico.

# Extended MHD Modeling of Tearing-Driven Magnetic Relaxation

J. P. Sauppe<sup>1,2, a)</sup> and C. R. Sovinec<sup>1,3, b)</sup>

<sup>1)</sup>*Center for Plasma Theory and Computation, 1500 Engineering Drive, Madison, WI 53706, USA*

<sup>2)</sup>*Department of Physics, University of Wisconsin-Madison, 1150 University Avenue, Madison, WI 53706, USA*

<sup>3)</sup>*Department of Engineering-Physics, University of Wisconsin-Madison, 1500 Engineering Drive, Madison, WI 53706, USA*

Discrete relaxation events in reversed-field pinch relevant configurations are investigated numerically with nonlinear extended magnetohydrodynamic modeling, including the Hall term in Ohm's law and first-order ion finite Larmor radius effects. Results show variability among relaxation events, where the Hall dynamo effect may help or impede the MHD dynamo effect in relaxing the parallel current density profile. The competitive behavior arises from multi-helicity conditions where the dominant magnetic fluctuation is relatively small. The resulting changes in parallel current density and parallel flow are aligned in the core, consistent with experimental observations. Analysis of simulation results also confirms that force density from fluctuation-induced Reynolds stress arises subsequent to the drive from fluctuation-induced Lorentz force density. Transport of momentum density is found to be dominated by the fluctuation-induced Maxwell stress over most of the cross section with viscous and gyroviscous contributions being large in the edge region.

## I. INTRODUCTION

Magnetic self-organization in the reversed-field pinch<sup>1</sup> (RFP) occurs in discrete relaxation events as a result of the nonlinear interaction of magnetohydrodynamic (MHD) fluctuations. Parallel current is preferentially driven in the core due to the magnetic winding of the RFP. The driven current profile provides a large source of free energy for core-resonant  $m = 1$  tearing modes,<sup>2</sup> resistive instabilities that bend and reconnect magnetic field lines. These tearing modes saturate nonlinearly by coupling to edge resonant  $m = 0$  modes and by redistributing the parallel current density through dynamo electric fields that result from correlated plasma fluctuations. In driven plasma pinch configurations like the RFP, relaxation often occurs quasi-periodically as the inductive drive and resistive diffusion gradually rebuild the peaked current density profile.<sup>3</sup> Measurements on the Madison Symmetric Torus<sup>4</sup> (MST) RFP also show changes in the plasma momentum density profile as another result of the discrete current relaxation events.<sup>5,6</sup> The coupling of current relaxation and momentum evolution is not predicted with the single-fluid MHD model, but extended MHD effects provide at least a qualitative description of this coupling.

Here, we examine how plasma fluctuations redistribute parallel current density and parallel flow during discrete relaxation events in single- and two-fluid numerical models of relaxation dynamics with and without ion gyroviscosity, a first-order ion finite Larmor radius (FLR) effect. Our primary goal is to understand the coupling between the current density and plasma flow during relaxation. This effort builds on previous numerical results which demonstrate changes in plasma flow associated with current relaxation within an extended MHD model.<sup>7</sup> Our computations are run with greater dissipation than those in Ref. 7, allowing simulation through multiple discrete relaxation events with three different models. Importantly, we find substantial differences between the dynamo electric fields during the initial relaxation event and subsequent events in our computations with extended MHD effects. The differences have significant implications for the coupling of current relaxation and flow evolution. Additionally, changes in axial and angular plasma momentum are observed with two-fluid models, and we diagnose both the source and the causes of the resulting radial transport.

Early analytical work identified the possibility of dynamo electric fields from correlated fluctuations of velocity and magnetic field, what is known as the single-fluid MHD dynamo,  $-\langle \tilde{\mathbf{V}} \times \tilde{\mathbf{B}} \rangle$ .<sup>8</sup> Helically symmetric MHD computations and comparison to Kadomtsev's sawtooth model clarified the nonlinear dynamics of isolated, tearing-driven magnetic islands in RFP configurations.<sup>9</sup> Subsequent studies highlight the importance of the MHD dynamo in quasi-linear analysis<sup>10</sup> and in 3D nonlinear computations.<sup>11</sup> The characteristic reversed-field state can be described by fluctuation-induced turbulence<sup>12</sup> and by reconnection of a magnetic island associated with an edge-resonant tearing mode that is driven nonlinearly by the core-resonant modes.<sup>13</sup> Other numerical studies highlight the importance of nonlinear

---

<sup>a)</sup>Presently at Los Alamos National Laboratory, Los Alamos, NM 87545, USA; Electronic mail: jpsauppe@lanl.gov

<sup>b)</sup>Electronic mail: csovinec@wisc.edu

interaction and find that the redistribution of current is mediated via three-wave coupling between core-resonant and edge-resonant tearing modes.<sup>14,15</sup>

Experimental measurements on MST substantiate the fluctuation-induced MHD dynamo during relaxation. Correlation of probe-measured magnetic and electrostatic fluctuations shows MHD dynamo activity of sufficient strength to sustain edge parallel current in early MST discharges.<sup>16</sup> Edge magnetic field fluctuations correlated with chordal spectroscopic measurements of velocity fluctuations also indicate significant contributions from the single-fluid MHD dynamo in the core.<sup>17</sup> Optical probe measurements find that the substantial contributions to MHD dynamo in the edge vanish near the reversal surface,<sup>18</sup> and this suggests the existence of an additional dynamo mechanism.

The possibility of non-MHD dynamo effects is evident when examining the generalized Ohm's law:

$$\mathbf{E} = -\mathbf{V} \times \mathbf{B} + \eta \mathbf{J} + \Lambda_e \left[ \frac{\mathbf{J} \times \mathbf{B}}{ne} - \frac{\nabla p_e}{ne} + \frac{m_e}{ne^2} \frac{\partial \mathbf{J}}{\partial t} \right]. \quad (1)$$

Here, the marker  $\Lambda_e$  is inserted to indicate where two-fluid effects enter the generalized Ohm's law;  $\Lambda_e = 0$  for single-fluid MHD while  $\Lambda_e = 1$  for two-fluid models. The Hall dynamo is identified as the result of correlated fluctuations of current density and magnetic field,  $\langle \tilde{\mathbf{J}} \times \tilde{\mathbf{B}} \rangle / \langle n \rangle e$ .<sup>19</sup> Nonlinear computations utilizing this extended MHD Ohm's law find significant contributions from both MHD dynamo and Hall dynamo in single-helicity<sup>20</sup> and multi-helicity<sup>7</sup> conditions.

Correlated fluctuations of density and electron temperature gradients may provide an additional dynamo electric field,<sup>21</sup> but this effect is found to be negligible in the computations presented here. The electron inertia term provides a resonance condition for the whistler wave at the electron cyclotron frequency, and it is included here to limit the range of temporal scales as spatial resolution is increased.<sup>22</sup> It also allows collisionless reconnection when the tearing layer approaches the electron skin depth,<sup>23,24</sup> but this is not measured to be significant in our computations.

Measurements on MST find that the Hall dynamo is negligible compared to the MHD dynamo near the plasma edge.<sup>25</sup> However, significant contributions to Hall dynamo electric field from the core-resonant tearing mode are identified using laser Faraday rotation, and the contributions are interpreted as being localized near the resonant surface.<sup>26,27</sup> More recent probe measurements near the plasma edge find Hall dynamo electric field that is large near the reversal surface,<sup>6</sup> where MHD dynamo is observed to vanish.<sup>18</sup> Development of a deep insertion probe allows a radial reconstruction of the Hall dynamo electric field across a much larger portion of the outer radius, and recent results indicate that the Hall dynamo electric field has regions of greater magnitude at smaller radii.<sup>28</sup>

Correlated fluctuations of current density and magnetic field also appear in the plasma momentum equation,

$$m_i n \frac{\partial \mathbf{V}}{\partial t} = -m_i n \mathbf{V} \cdot \nabla \mathbf{V} + \mathbf{J} \times \mathbf{B} - \nabla p - \nabla \cdot \underline{\Pi}_i, \quad (2)$$

as a Lorentz force density, and two-fluid effects naturally couple the current and momentum evolution. Experimental measurements of the Hall dynamo and associated Lorentz force density near the edge during relaxation find it is nearly balanced by the fluid response through the force density from Reynolds stress.<sup>6</sup> However, significant changes in plasma momentum density parallel to the large-scale magnetic field are observed at the discrete relaxation events. The changes are in the direction of the Lorentz force density, as might be expected for a system where magnetic energy density dominates.

A previous computational study demonstrates the two-fluid coupling of current and flow evolution during relaxation, and it reproduces the balancing between the fluctuation-induced Lorentz force density and fluid response with net changes in plasma flow in the direction of Lorentz force density.<sup>7</sup> In Ref. 7 the current density is parallel to the magnetic field,  $\mathbf{J} \cdot \mathbf{B} > 0$ , and the change in parallel current density and the change in parallel flow in the core are in opposite directions during the examined relaxation events. However, standard operation of MST has  $\mathbf{J} \cdot \mathbf{B} < 0$ , and the experimental results of Ref. 6 find that relaxation-induced changes in parallel current density and parallel flow in the core are in the same direction. This is observed to hold in ensemble-averaged experimental results, regardless of the sign of  $\mathbf{J} \cdot \mathbf{B}$ . As described in Sec. III D, reversing the sign of  $\mathbf{J} \cdot \mathbf{B}$  in the computations still results in the relaxation-induced change in parallel current density opposing the relaxation-induced change in parallel flow during the first relaxation event of a simulation.

The remainder of the paper is organized as follows. In Sec. II, we introduce the extended MHD models used here and describe the initial and boundary conditions for our computations. Computational results are presented in Sec. III, and we focus primarily on the dynamo electric fields, plasma flow evolution, and changes in total axial and angular momentum during relaxation. A brief discussion and concluding remarks are given in Sec. IV.

## II. EXTENDED MHD MODEL

### A. Modeling

We investigate plasma relaxation dynamics numerically with the NIMROD code, which is used to solve extended MHD systems of equations.<sup>22,29</sup> The magnetic field is advanced using Faraday's law without displacement current, as appropriate for the low-frequency dynamics under investigation here,

$$\frac{\partial \mathbf{B}}{\partial t} = -\nabla \times \mathbf{E} + \kappa \nabla (\nabla \cdot \mathbf{B}), \quad (3)$$

and the electric field is given by Eq. (1). A divergence cleaning term is needed in the magnetic field advance, as the NIMROD representation does not satisfy  $\nabla \cdot \mathbf{B} = 0$  identically.<sup>29</sup> However, Ref. 30 shows that the residual numerical error does not appreciably affect the computations presented here.

When solving Eq. (2) for flow velocity, the anisotropic stress tensor in our computations consists of a simple viscous term and the Braginskii gyroviscous term:

$$\underline{\Pi}_i \equiv \underline{\Pi}_{\text{iso}} + \Lambda_i \underline{\Pi}_{\text{gyr}}. \quad (4)$$

Here, the marker  $\Lambda_i$  is used to indicate where ion FLR effects enter the system;  $\Lambda_i = 0$  when they are excluded and  $\Lambda_i = 1$  when they are included. The collisional viscosity is modeled as  $\underline{\Pi}_{\text{iso}} = \nu m_i n \underline{\mathbf{W}}$ , where  $\underline{\mathbf{W}} = \nabla \mathbf{V} + (\nabla \mathbf{V})^T - \frac{2}{3} \mathbf{I} (\nabla \cdot \mathbf{V})$ . Ion FLR effects enter the system at the same order as the extended MHD effects in Ohm's law if the ions are not cold, and they can be included to first order via the Braginskii ion gyroviscous stress tensor,<sup>31</sup>

$$\underline{\Pi}_{\text{gyr}} = \frac{m_i p_i}{4e |\mathbf{B}|} \left[ \hat{\mathbf{b}} \times \underline{\mathbf{W}} \cdot (\mathbf{I} + 3\hat{\mathbf{b}}\hat{\mathbf{b}}) - (\mathbf{I} + 3\hat{\mathbf{b}}\hat{\mathbf{b}}) \cdot \underline{\mathbf{W}} \times \hat{\mathbf{b}} \right] \quad (5)$$

where  $\hat{\mathbf{b}} \equiv \mathbf{B}/|\mathbf{B}|$ .

The continuity equation includes a small artificial diffusion for numerical stability,

$$\frac{\partial n}{\partial t} = -\nabla \cdot (n \mathbf{V}) + \nabla \cdot (D_n \nabla n), \quad (6)$$

but it does not significantly affect the dynamics of interest here. We model the electrons and ions as being at fixed fractions of a single temperature,  $T_i = f_{T_i} T$  and  $T_e = (1 - f_{T_i}) T$ , where  $f_{T_i}$  represents the ion temperature fraction. Detailed thermal transport modeling is beyond the scope of this work, so viscous and Ohmic heating are neglected in the temperature advance,

$$n \frac{\partial T}{\partial t} = -n \mathbf{V} \cdot \nabla T - n T (\Gamma - 1) \nabla \cdot \mathbf{V} + \nabla \cdot (\chi n \nabla T), \quad (7)$$

and a simple isotropic thermal conduction is used.

We approximate the RFP geometry as a periodic cylinder with minor radius  $a$ , axial length  $L = 2\pi R$ , and aspect ratio  $R/a = 3$ , which roughly matches MST. NIMROD utilizes a spectral-element expansion<sup>29</sup> for two spatial directions and a Fourier representation in the third periodic direction. Here, the spectral elements are used for the radial ( $r$ ) and axial ( $z$ ) directions, and periodic boundary conditions are imposed in the axial direction to yield a topologically toroidal domain. Regularity conditions are enforced at  $r = 0$ , and the boundary conditions enforced at  $r = a$  are discussed in Sec. II B. The  $r - z$  plane is discretized with a rectangular grid consisting of uniformly spaced elements in the radial and axial directions, with basis functions of fixed polynomial degree within each element. All computations reported here have a  $120 \times 64$  (radial  $\times$  axial) mesh of biquintic finite elements. Convergence has been ascertained, in part, by comparison to computations run with bicubic elements for the same conditions, as discussed in greater detail in Appendix A of Ref. 30. A finite Fourier series is used to represent the azimuthal (poloidal) angle ( $\theta$ ), and the computations here use 6 harmonics,  $0 \leq m \leq 5$ , where  $m$  is the poloidal harmonic number. This poloidal resolution is sufficient to capture the dominant low- $m$  activity during relaxation events in the RFP. The magnetic energy in the largest resolved Fourier harmonic ( $m = 5$ ) is typically 3 orders of magnitude smaller than the energy in the dominant  $m = 1$  component during relaxation events.

### B. Initial and Boundary Conditions

Our RFP computations are initialized from a force-free paramagnetic pinch,  $\mathbf{J} \times \mathbf{B}|_{t=0} = \nabla p|_{t=0} = \mathbf{0}$ , with finite plasma pressure. The paramagnetic pinch is an Ohmic steady state that is sustained by an externally applied electric

TABLE I. Parameters of models used in our computations.

Model	$\Lambda_e$	$\Lambda_i$	$S$	$a\lambda(0)$
A	0	0	20000	-3.88
B	1	0	20000	-3.88
C	1	1	20000	-3.88

field,  $\mathbf{E}|_{t=0} = -\mathbf{V} \times \mathbf{B}|_{t=0} + \eta \mathbf{J}|_{t=0}$ , with  $\nabla \times \mathbf{E}|_{t=0} = \mathbf{0}$ .<sup>32</sup> The state includes a small inward pinch flow that is directly proportional to resistivity, but contributions from this term are neglected in the density [Eq. (6)] and velocity [Eq. (2)] advances. As discussed in Sec. III E, this results in an anomalous sink of momentum, but it does not significantly affect the evolution of plasma flow in the core, where the pinch flow is small. Our computations do not include any initial axial or angular flow profile; our focus here is solely on changes in plasma flow associated with the discrete current relaxation events. Small perturbations to the magnetic field and flow that are several orders of magnitude smaller than the axisymmetric fields described above are imposed to excite linearly unstable tearing modes.

No-slip boundary conditions are imposed on the tangential components of plasma flow, and the normal component of magnetic field is held fixed,  $\mathbf{B} \cdot \hat{\mathbf{n}}|_{r=a} = 0$ . Dirichlet boundary conditions are applied to the temperature,  $T|_{r=a} = T|_{r=a,t=0}$ , allowing thermal energy to flow into and out of the system at a rate limited by the isotropic thermal conductivity. The artificial density diffusion allows one to utilize similar boundary conditions for the number density,  $n|_{r=a} = n|_{r=a,t=0}$ , and particles may enter or exit the computational domain at a rate limited by the density diffusion coefficient.

### C. Parameters

Our model system [Eqs. (1)-(7)] may be parametrized by seven dimensionless physical parameters and two numerical parameters. The characteristic length scale is taken to be the plasma minor radius  $a$ . The seven physical parameters are (1) the Lundquist number, the ratio of the resistive diffusion time and the Alfvén time,  $S = \tau_R/\tau_A$ , where  $\tau_A = a\sqrt{\mu_0 m_i n}/|\mathbf{B}|$  and  $\tau_R = \mu_0 a^2/\eta$ ; (2) the magnetic Prandtl number, the ratio of resistive and viscous times,  $P_m = \tau_R/\tau_\nu$ , where  $\tau_\nu = a^2/\nu$ ; (3) the ratio of the viscous and thermal conduction times,  $\tau_\nu/\tau_\chi = \chi/\nu$ ; (4) the plasma- $\beta$ , the ratio of fluid and magnetic pressures,  $\beta = 2\mu_0 p/B^2$ ; (5) the ion temperature fraction  $f_{T_i}$ ; (6) the normalized ion skin depth,  $d_i/a = c/\omega_{p_i} a = \sqrt{m_i/\mu_0 n e^2}/a$ ; and (7) the normalized electron skin depth,  $d_e/a = c/\omega_{p_e} a = \sqrt{m_e/m_i} d_i/a$ , which can be varied artificially by changing the mass ratio  $m_e/m_i$ . The two numerical parameters are (1) the ratio of viscous to density diffusion times,  $\tau_\nu/\tau_{D_n} = D_n/\nu$ ; and (2) the ratio of divergence cleaning to resistive diffusion times,  $\tau_{\nabla \cdot \mathbf{B}}/\tau_R = \eta/\mu_0 \kappa$ .

All computations presented here have a Lundquist number  $S = 20000$ , which is roughly 2 orders of magnitude smaller than in the experiment, as limited by computational practicalities. The isotropic viscosity is of the same order as resistivity,  $P_m = 1.0$ . As an idealization in our computations, both the resistivity and viscosity profiles are essentially uniform; they rise sharply only near  $r = a$ . This is in contrast to experiments, where the resistivity increases more gradually as plasma temperature decreases from the core to the edge. The isotropic thermal conduction is one order of magnitude smaller,  $\tau_\nu/\tau_\chi = 0.1$ , and it is spatially uniform with no dependence on temperature. The fluid pressure is slightly higher than in the MST experiment, and  $\beta = 0.10$  on-axis. As noted previously, the pressure profile is uniform in our computations to focus on the current-gradient-driven tearing dynamics. However, the ion skin depth is comparable to values inferred in MST,  $d_i/a \approx 0.17$ . The ion and electron temperatures are assumed to be equal,  $f_{T_i} = 0.5$ . The electron mass is artificially increased by a factor of 5 for numerical convenience,  $m_e/m_i \approx 2.72 \cdot 10^{-3}$ . Lastly, the numerical parameters for our computations are  $\tau_\nu/\tau_{D_n} = 0.1$  and  $\tau_{\nabla \cdot \mathbf{B}}/\tau_R = 5 \cdot 10^{-5}$ .

We consider computations for each of the three sets of dimensionless parameters that are summarized in Table I. The evolution of magnetic helicity, hybrid helicity, and magnetic energy for these cases is analyzed in Ref. 30. The first model (A) uses the standard magnetohydrodynamic Ohm's law ( $\Lambda_e = 0$ ) and excludes the ion gyroviscous stress tensor ( $\Lambda_i = 0$ ). The other two models incorporate two-fluid effects in the generalized Ohm's law ( $\Lambda_e = 1$ ). The second model (B) does not include the gyroviscous stress tensor ( $\Lambda_i = 0$ ), while the third (C) does ( $\Lambda_i = 1$ ). The dimensionless parallel current density,  $a\lambda = a\mu_0 \mathbf{J} \cdot \mathbf{B}/|\mathbf{B}|^2$ , has an on-axis value of  $a\lambda(0) = -3.88$  in all our computations, and this is similar to standard operation of the MST experiment which has  $-4 \leq a\lambda(0) \leq -3$ .

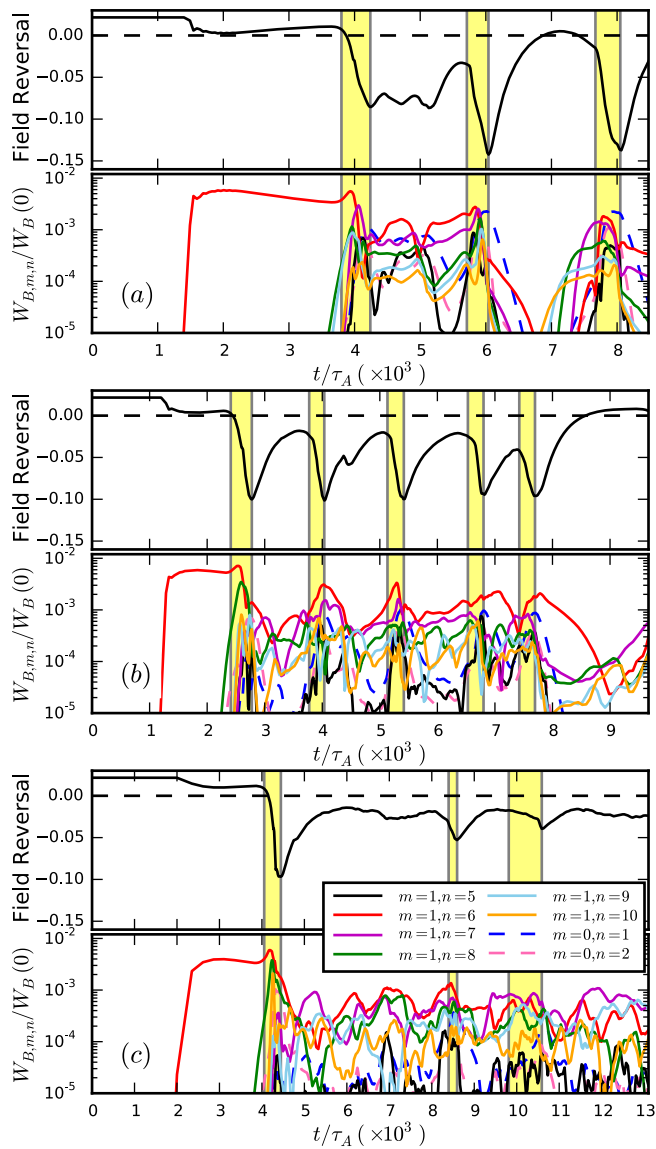


FIG. 1. Field reversal parameter and normalized spectral magnetic energy  $W_{B,m,n}(t)/W_{B,0,0}(0)$  in (a) case A: single-fluid MHD ( $\Lambda_e = 0$ ,  $\Lambda_i = 0$ ), (b) case B: two-fluid no gyroviscosity ( $\Lambda_e = 1$ ,  $\Lambda_i = 0$ ), (c) case C: two-fluid with gyroviscosity ( $\Lambda_e = 1$ ,  $\Lambda_i = 1$ ). Relaxation events are highlighted.

### III. RESULTS

#### A. Global Evolution

Our computations display multiple discrete relaxation events during the nonlinear evolution, as indicated by the highlighted regions in Fig. 1. The upper plot for each computation shows the field reversal parameter,  $F = \langle B_z \rangle_{r=a} / \langle B_z \rangle_{\text{vol}}$ , the average toroidal field at the wall of the device divided by the average toroidal field over the volume, and the lower plots show the evolution of the largest magnetic fluctuation energies, normalized to the initial axisymmetric magnetic energy. Relaxation events in our computations are characterized by an increase in the level of field reversal and a high level of magnetic fluctuation energy in multiple helical components. The increase in depth of reversal is a characteristic of experimental relaxation events,<sup>4</sup> and measurements of the magnetic fluctuation amplitudes at the wall of the device<sup>27,33</sup> show increased activity during relaxation, similar to our volume-integrated magnetic energies. Each event typically ends with a peaking of magnetic energy in the edge resonant  $m = 0$  modes as the  $m = 1$  mode energies begin to fall off.

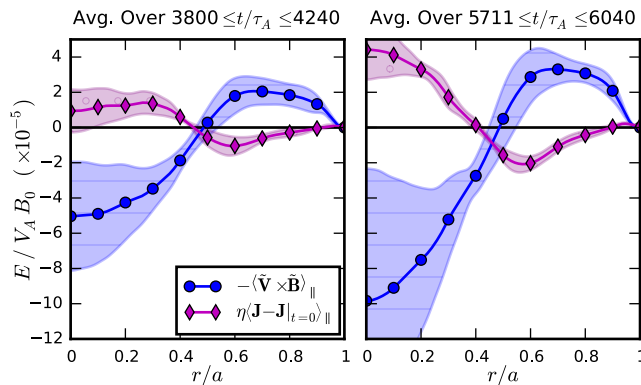


FIG. 2. Dynamo electric field averaged over two relaxation events in case A ( $\Lambda_e = 0$ ,  $\Lambda_i = 0$ ), the single-fluid MHD computation. The lines indicate the temporal average, and the shaded regions indicate  $\pm$  one standard deviation.

Each computation begins from the perturbed paramagnetic pinch state and evolves into a saturated quasi-single-helicity<sup>34,35</sup> (QSH) state dominated by the fastest-growing core-resonant  $m = 1, n = 6$  mode. The initial relaxation event disrupts this QSH state once additional tearing modes grow to appreciable amplitude. We identify the beginning of the first event as when the slower-growing modes contain approximately 5% of the energy of the dominant mode. In the single-fluid MHD computation, the QSH state persists for about  $2500 \tau_A$ . That period is shorter for the extended-MHD computations. In the absence of drift effects, two-fluid effects enhance linear tearing growth rates, relative to resistive-MHD, when the resistive layer width is smaller than the ion sound gyroradius,  $\rho_s = \sqrt{\Gamma\beta/2}d_i$ .<sup>36,37</sup> This effect can shorten the time it takes for the other linearly unstable modes in cases B and C to compete with the  $m = 1, n = 6$  mode. However, warm-ion gyroviscous effects representing  $\nabla|\mathbf{B}|$  and poloidal-curvature drifts reduce tearing-mode growth rates.<sup>20</sup> That the QSH state persists for only  $1100 \tau_A$  in case B and slightly longer,  $2000 \tau_A$ , in our case C is, therefore, consistent with the tearing growth-rates from the different models. The end of the relaxation event is determined when the field reversal parameter reaches a minimum. The initial relaxation events in our computations here are qualitatively consistent with the initial events reported in Ref. 7.

Following the initial event, the magnetic energy in the fluctuations remains at a modest level in a multi-helicity state. Subsequent relaxation events occur from these conditions and are identified, in part, based on significant nonlinear correlations evidenced through dynamo activity. These events typically begin when core-resonant modes again grow to appreciable amplitude. Nonlinear coupling between these modes and the edge resonant  $m = 0$  modes drives higher  $n$  modes, and the parallel current density is redistributed from the core region to the edge region, flattening the gradient and reducing the source of free energy. The relaxation events end with a peaking of magnetic energy in the edge resonant modes and a rapid reduction in energies of the core modes.

Before proceeding further, we first draw a distinction between the subsequent events identified in our computations and those of Ref. 7. In the subsequent events identified in that work, the  $m = 0$  amplitude remained small, a fact that was attributed to a lack of nonlinear drive rather than a direct result of gyroviscous stabilization. In the subsequent events we have identified here, we find significant nonlinear drive of the  $m = 0$  mode and consequently larger changes in field reversal parameter. Our case C computation is comparable to the two-fluid computations discussed in Ref. 7; the largest differences are that our computation is run at  $S = 20000$  instead of  $S = 80000$ , and it has greater spatial resolution. The second large-scale relaxation event in our case C computation occurs nearly  $4000 \tau_A$  after the initial event, roughly  $1/5$  of a resistive diffusion time, which for  $S = 80000$  corresponds to  $16000 \tau_A$ . The computation of Ref. 7 is run out for  $8000 \tau_A$ , so it is possible that subsequent large scale relaxation events would also be observed at later times in that case.

## B. Dynamo Electric Fields

Current density is redistributed through dynamo electric fields parallel to  $\langle \mathbf{B} \rangle$ , and here we examine their behavior in the initial and subsequent events of our three computations. The MHD dynamo has a consistent radial structure in all of the relaxation events in our single-fluid MHD computation (case A), as can be seen in Fig. 2, which shows the dynamo electric fields in the first and second relaxation events. (The third event is similar in character to the second and is not shown here.) The solid lines show the temporal average over the duration of the event, while the shaded regions indicate the standard deviation. The MHD dynamo is negative in the core and positive near the edge, changing sign near  $r/a \sim 0.5$ , and acting to flatten the parallel current profile in each event. In the subsequent

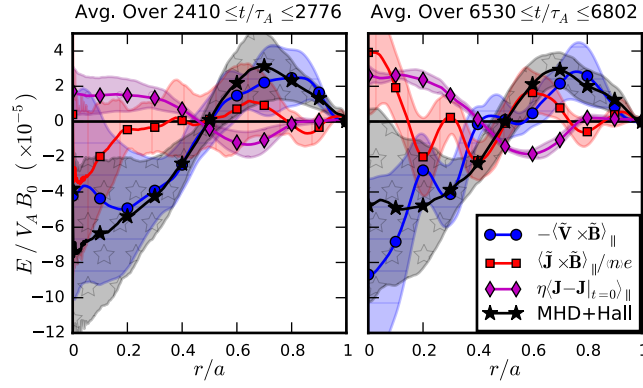


FIG. 3. Dynamo electric fields averaged over two relaxation events in case B ( $\Lambda_e = 1$ ,  $\Lambda_i = 0$ ), the two-fluid computation without ion gyroviscosity.

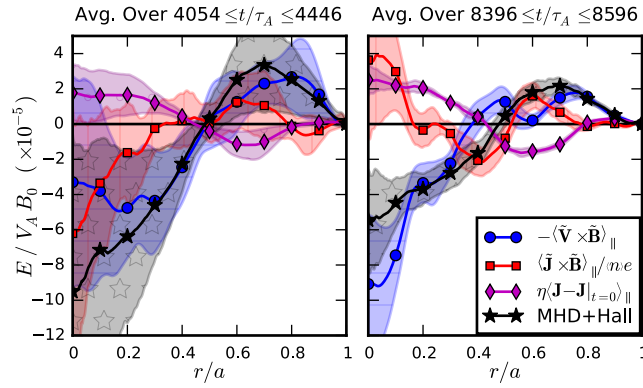


FIG. 4. Dynamo electric fields averaged over two relaxation events in case C ( $\Lambda_e = 1$ ,  $\Lambda_i = 1$ ), the two-fluid computation with ion gyroviscosity.

relaxation events, the amplitude of the MHD dynamo is roughly twice as large as it is in the initial event. This correlates well with the larger changes in the parallel current density profile, evident in the  $\eta \langle \mathbf{J} - \mathbf{J}|_{t=0} \rangle_{||}$  term, and the increased depth of reversal observed in these later events.

The two-fluid Hall dynamo is comparable in magnitude to the MHD dynamo in our computations that include two-fluid effects in the model. In the absence of ion gyroviscosity (case B), the two-fluid Hall dynamo is largest in the initial relaxation event and the fourth event, shown in Fig. 3. In the other relaxation events, the Hall dynamo has considerable temporal variation, and the averages over the relaxation events remain small. Both MHD and Hall dynamos are large during the first and second relaxation events in our two-fluid computation with ion gyroviscosity (case C), as can be seen in Fig. 4. The third relaxation event in case C is significantly weaker, evident in the smaller drop in field reversal, although the dynamo electric field structure is comparable to the second event.

In the first relaxation event of both two-fluid computations, the MHD dynamo and Hall dynamo act to flatten the parallel current profile, each being negative in the core and positive near the edge. This behavior is in qualitative agreement with previous two-fluid computations that also find the two dynamo effects acting constructively during the initial event.<sup>7</sup> However, in some of the subsequent relaxation events in our computations, most notably in the fourth relaxation event of case B and in both subsequent events of case C, the two dynamo effects oppose each other. The MHD dynamo always acts to relax the parallel current profile, and the Hall dynamo is found to sometimes oppose this relaxation, although it remains weaker in amplitude. Consequently, in all cases, the total dynamo acts to relax the parallel current profile, and  $\Delta \langle \mathbf{J} \rangle_{||}$  is always positive in the core for these negative- $\lambda$  computations. As described in Sec. III D, the dynamo competition in the core region results in  $\Delta \langle \mathbf{J} \rangle_{||}$  and  $\Delta \langle \mathbf{V} \rangle_{||}$  being in the same direction, consistent with experimental measurements. The dynamo activity in the edge region ( $0.5 < r/a < 1$ ) of all events tends to alternate over  $r$  between the two effects to relax the parallel current profile there. Possible causes of the dynamos acting in opposition are addressed in Sec. III C.

The sum of the MHD and Hall dynamos can be expressed in terms of an electron fluid velocity,

$$-\langle \tilde{\mathbf{V}} \times \tilde{\mathbf{B}} \rangle_{\parallel} + \frac{1}{\langle n \rangle e} \langle \tilde{\mathbf{J}} \times \tilde{\mathbf{B}} \rangle_{\parallel} \approx -\langle \tilde{\mathbf{V}}_e \times \tilde{\mathbf{B}} \rangle_{\parallel}. \quad (8)$$

To the extent that non-ideal terms in the generalized Ohm's law [Eq. (1)] remain small, the magnetic field can be considered to be frozen into the electron fluid. It is interesting to note that in all of the relaxation events of our two-fluid computations, this sum is found to be very similar to the MHD dynamo from our single-fluid computations. That is, radial variations in the Hall dynamo and MHD dynamo in our two-fluid computations appear to complement each other in such a way that the total dynamo is similar to the dynamo from single-fluid MHD.

Lastly, note that dynamo terms involving density fluctuations in the Hall term are also possible in our two-fluid model,

$$\begin{aligned} \left\langle \frac{\mathbf{J} \times \mathbf{B}}{ne} \right\rangle_{\parallel} &= \frac{\langle \tilde{\mathbf{J}} \times \tilde{\mathbf{B}} \rangle_{\parallel}}{\langle n \rangle e} - \frac{(\langle \mathbf{J} \rangle \times \langle \tilde{n} \tilde{\mathbf{B}} \rangle)_{\parallel}}{\langle n \rangle^2 e} \\ &\quad - \frac{\langle \tilde{n} \tilde{\mathbf{J}} \times \tilde{\mathbf{B}} \rangle_{\parallel}}{\langle n \rangle^2 e} + \mathcal{O} \left( \left( \frac{\tilde{n}}{\langle n \rangle} \right)^2 \right). \end{aligned} \quad (9)$$

However, we find that the difference between the total [LHS of Eq. (9)] and the first term on the RHS of Eq. (9) is less than 1% in our computations. The second term on the RHS of Eq. (9) may have a larger effect if a realistic pressure profile, with more significant  $\langle \mathbf{J} \rangle_{\perp}$ , is used.

### C. Dynamo Opposition

Hall and MHD dynamo effects acting in opposition in some subsequent relaxation events in our two-fluid computations results from several factors. First, all subsequent relaxation events have significant contributions from additional modes that are not active during the initial relaxation event. As noted previously, the initial event disrupts a quasi-single-helicity state, which is dominated by the  $m = 1, n = 6$  mode, while the subsequent events occur from multi-helicity conditions that are believed to be more representative of conditions prior to most events in conventional RFP experiments.

This distinction can be readily seen in Figs. 5 and 6, which show the modal decomposition of the dynamo electric fields averaged over representative relaxation events in our cases B and C, respectively. In the first event of both two-fluid computations, the MHD and Hall dynamo electric fields are dominated by contributions from just the core-resonant  $m = 1, n = 6$  mode with minor contributions from the  $m = 1, n = 8$  mode. However, in the subsequent events, there are additional large contributions to the dynamo electric fields from both the  $m = 1, n = 5$  mode and the  $m = 1, n = 7$  mode. Importantly, the contributions to the Hall dynamo from these two modes are often found to oppose current relaxation in the core, and this is at least partially responsible for the change in sign of the total Hall dynamo.

We also find that core Hall dynamo opposition to MHD dynamo in subsequent events is strongly correlated with reduced  $m = 1, n = 6$  magnetic energy and correspondingly smaller contributions to the Hall dynamo. In our two-fluid computation with ion gyroviscosity, the Hall dynamo is opposed to the MHD dynamo in both of the subsequent relaxation events. The magnetic energy in the  $m = 1, n = 6$  mode in the second event is  $\sim 23\%$  of the maximum in the first event, and it is  $\sim 12\%$  in the third event. Contributions to the Hall dynamo in the core from the  $m = 1, n = 6$  mode drop significantly in these subsequent relaxation events. In contrast, in our two-fluid computations without ion gyroviscosity (case B), dynamo opposition is only observed in the fourth relaxation event, where the  $m = 1, n = 6$  mode magnetic energy peaks at roughly 26% of its maximum in the quasi-single-helicity event. In the second and third events of this computation, the  $m = 1, n = 6$  mode magnetic energy is significantly larger, being 44–45% of the initial event, and there is a correspondingly larger contribution to the Hall dynamo from this mode.

The smaller amplitudes of the  $m = 1, n = 6$  mode magnetic energies in our case C computation may be attributed to gyroviscous stress. Its effect on linear growth-rates is greatest for intermediate values of  $k\rho_s$ , as kinetic Alfvén wave tearing becomes predominant at higher  $k$ .<sup>20</sup> Our computations have a flat pressure profile, and the magnetic energy density decreases with radius, so  $\rho_s$  increases with  $r/a$ . Combining this with the increasing  $k$  as the safety factor profile falls off, we find that  $k\rho_s$  becomes much larger and the gyroviscous stabilization becomes much less important as we move from core to edge. However, a more realistic pressure profile, with decreasing  $\rho_s$ , might at least partially compensate the increasing  $k$ , resulting in more gyroviscous stabilization for modes resonant near  $r/a \sim 0.5$ .

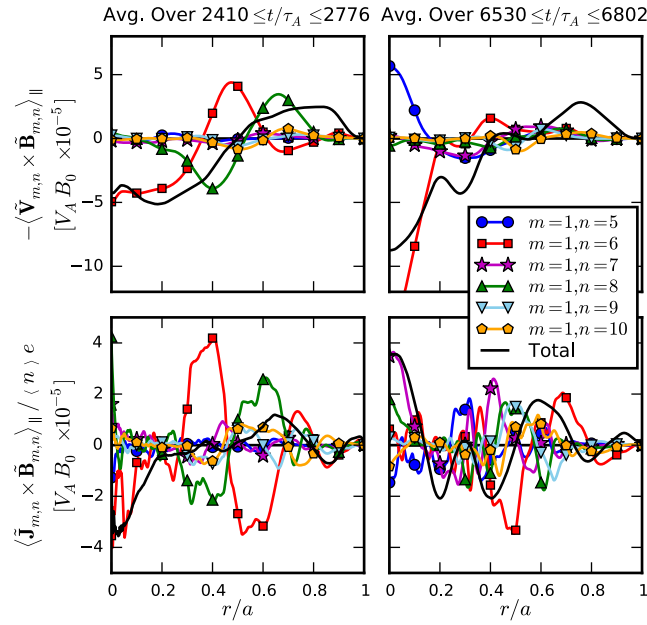


FIG. 5. Modal decomposition of dynamo electric fields averaged over two relaxation events in case B ( $\Lambda_e = 1$ ,  $\Lambda_i = 0$ ).

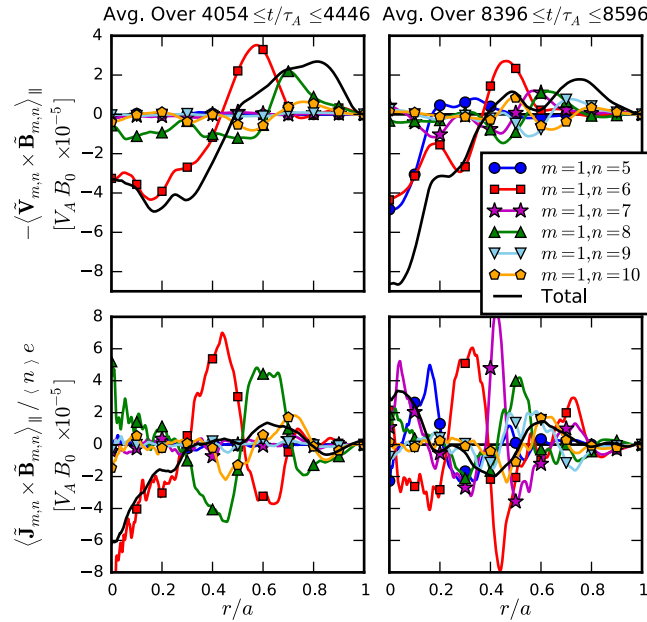


FIG. 6. Modal decomposition of dynamo electric fields averaged over two relaxation events in case C ( $\Lambda_e = 1$ ,  $\Lambda_i = 1$ ).

#### D. Flow Profile Evolution

As discussed in Sec. I, the Hall dynamo also manifests as a Lorentz force density in the plasma momentum equation. In our single-fluid MHD computations, the Hall dynamo is excluded from the model, and the fluctuation-induced Lorentz force density associated with the relaxation dynamics is weak. This is in agreement with previous single-fluid results reported in Ref. 7. In our two-fluid computations we find significant Lorentz force density associated with the current relaxation dynamics, as can be seen in Figs. 7 and 8, which show the radial structure of the axisymmetric force densities averaged over the relaxation events in cases B and C, respectively. In all of these events in our two-fluid computations, the Lorentz force density has essentially the same radial structure as the Hall dynamo, differing only by  $\langle n \rangle$ .

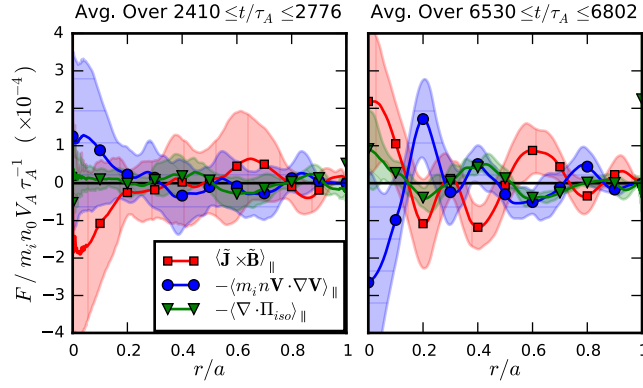


FIG. 7. Axisymmetric force densities averaged over two relaxation events in case B ( $\Lambda_e = 1$ ,  $\Lambda_i = 0$ ).

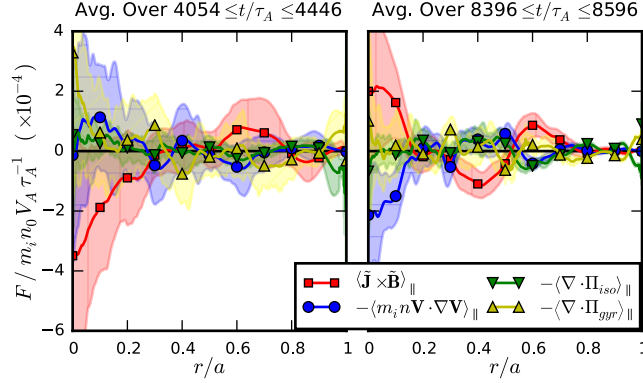


FIG. 8. Axisymmetric force densities averaged over two relaxation events in case C ( $\Lambda_e = 1$ ,  $\Lambda_i = 1$ ).

The Lorentz force density provides the largest contribution to parallel flow evolution during relaxation, but we also find a significant force density from Reynolds stress,  $-\langle m_i n \mathbf{V} \cdot \nabla \mathbf{V} \rangle_{\parallel}$ , which is an inertial effect, in agreement with both previous computations<sup>7</sup> and experimental measurements.<sup>6</sup> The Lorentz force density precedes the fluid response in both the core and the edge in our two-fluid computations without ion gyroviscosity, as evident in Fig. 9, and in our two-fluid computations with ion gyroviscosity, Fig. 10. The Lorentz force density also tends to be larger in magnitude, and changes in the parallel flow velocity tend to follow the radial structure of this term. Thus, the Lorentz force density drives the momentum density evolution as a result of the magnetic relaxation, and the inertial response arises primarily to counter this drive.

The intrinsic flow profile that appears in experiment between the relaxation events is believed to result from transport effects that are beyond the scope of our model. Nevertheless, the current relaxation dynamics are well represented, and we expect that changes in the flow profile associated with the current relaxation events are also captured in our two-fluid computations. The parallel flow profiles at the onset and end of relaxation, as well as the change over the relaxation event, are shown in Figs. 11 and 12, for our two-fluid computations without and with ion gyroviscosity, respectively.

The parallel flow generated in the core during the initial relaxation event in both two-fluid computations is in the opposite direction of experimental measurements, which are inferred from Fig. 4(a) of Ref. 6. The 200 kA discharges of Ref. 6 use an on-axis magnetic field of  $B_0 = 0.2$  T and a deuterium plasma with  $n_0 \approx 10^{19}$  m<sup>-3</sup> yielding an on-axis Alfvén velocity of  $V_A \approx 10^6$  m/s. We estimate  $\Delta \langle \mathbf{V} \rangle_{\parallel} / V_A = +0.014$ ,  $-0.011$ , and  $-0.018$ , at  $r/a = 0.30$ ,  $0.50$ , and  $0.66$ , respectively, at the relaxation event in experiment. These values are indicated by the stars in Figs. 11 and 12. The simulated flow-profile evolution reported in Ref. 7 is in qualitative agreement with these measurements, but the computations there are performed for  $\mathbf{J} \cdot \mathbf{B} > 0$ , while our computations and typical experimental conditions both have  $\mathbf{J} \cdot \mathbf{B} < 0$ . Reversing the direction of  $\mathbf{J} \cdot \mathbf{B}$  also reverses the relaxation-induced change in plasma flow during the initial event, and this is readily seen by comparing the first events of our computations (shown in Figs. 11 and 12) to Fig. 13(a) of Ref. 7.

The flow-profile evolution is markedly different in subsequent relaxation events of our computations where the MHD dynamo acts to flatten the parallel current density profile and the Hall dynamo acts in opposition to it. There, the

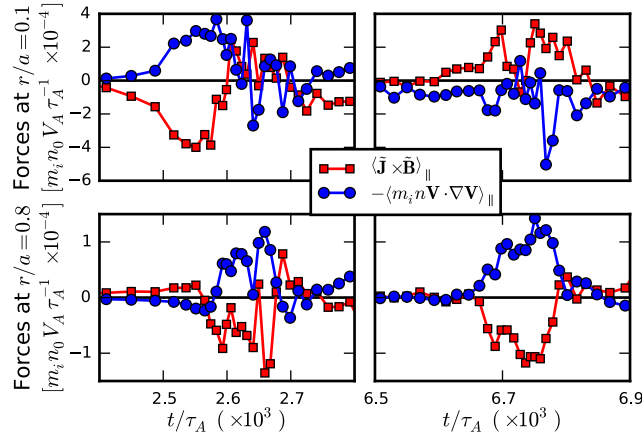


FIG. 9. Fluctuation-induced Lorentz force density and Reynolds force density in the core (top) and edge (bottom) regions during two relaxation events in case B ( $\Lambda_e = 1$ ,  $\Lambda_i = 0$ ).

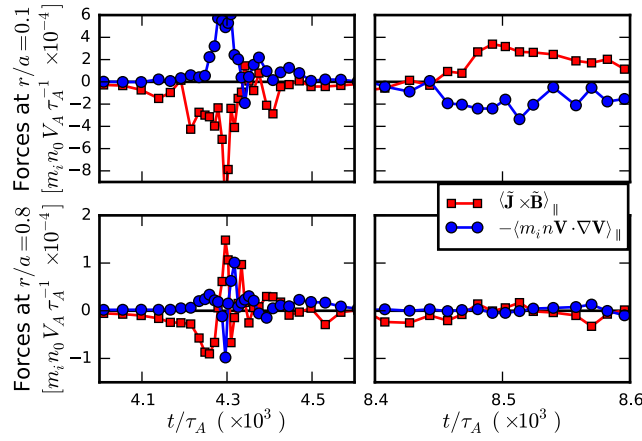


FIG. 10. Fluctuation-induced Lorentz force density and Reynolds force density in the core (top) and edge (bottom) regions during two relaxation events in case C ( $\Lambda_e = 1$ ,  $\Lambda_i = 1$ ).

relaxation-induced change in the parallel flow profile is more consistent with experimental observations, namely that changes in parallel plasma flow in the core are in the same direction as changes in parallel current density in the core.

Lastly, we note that our two-fluid computations have a much larger fraction of kinetic energy in flows that are perpendicular to the magnetic field, rather than parallel to it.<sup>30</sup> To lowest order in the ion skin depth, two-fluid variational theories predict a relaxed state with flow that is completely parallel to the magnetic field.<sup>38</sup> However, our computations, previous computational work,<sup>20</sup> and two-fluid variational theories carried out to higher order<sup>39</sup> indicate that perpendicular flows are also significant during relaxation.

### E. Momentum Transport

The total axial and angular momenta increase during relaxation events in our two-fluid computations, as can be seen in Fig. 13, whereas both remain relatively small in our single-fluid MHD computation. The momentum density,  $\mathbf{p} \equiv m_i n \mathbf{V}$ , in our computations evolves according to

$$\frac{\partial \mathbf{p}}{\partial t} \approx \nabla \cdot \left[ \frac{\mathbf{B}\mathbf{B}}{\mu_0} - m_i n \mathbf{V}\mathbf{V} - \left( \frac{|\mathbf{B}|^2}{2\mu_0} + p \right) \mathbf{I} - \underline{\mathbf{I}}_i \right], \quad (10)$$

where we have neglected small terms associated with the equilibrium pinch flow and density diffusion. The evolution of the axial momentum inside radius  $r$  (for  $0 \leq r \leq a$ ) is obtained by integrating the  $\hat{\mathbf{z}}$  projection of Eq. (10) over the

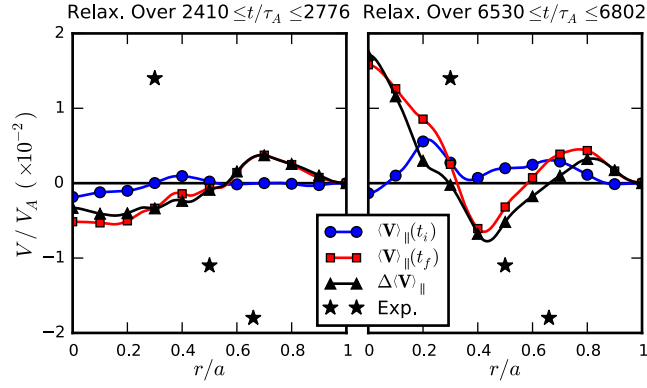


FIG. 11. Axisymmetric parallel flow before and after the relaxation events in case B ( $\Lambda_e = 1$ ,  $\Lambda_i = 0$ ).

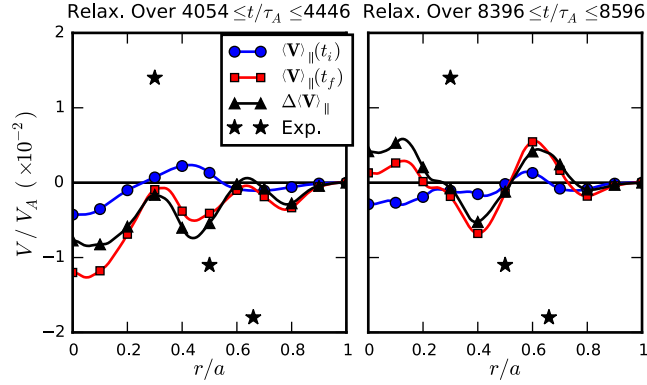


FIG. 12. Axisymmetric parallel flow before and after the relaxation events in case C ( $\Lambda_e = 1$ ,  $\Lambda_i = 1$ ).

volume of the cylinder of radius  $r$ :

$$\frac{\partial}{\partial t} \int m_i n \mathbf{V} \cdot \hat{\mathbf{z}} d^3 \mathbf{x} \equiv \frac{\partial}{\partial t} P_z(r) \approx \int dA \hat{\mathbf{r}} \cdot \left[ \frac{\mathbf{B}\mathbf{B}}{\mu_0} - m_i n \mathbf{V}\mathbf{V} - \underline{\underline{\Pi}}_i \right] \cdot \hat{\mathbf{z}}. \quad (11)$$

Similarly, the evolution of the angular momentum inside a finite volume is found by integrating the  $r\hat{\theta}$  projection of Eq. (10), taking care to include the geometric variation of  $\hat{\theta}$ . The evolution of the total axial and angular momentum,  $P_z(r=a)$  and  $P_\theta(r=a)$ , in our computations is shown in Fig. 13. The Maxwell and Reynolds stresses are associated with radial transport of momentum, and total axial and angular momentum are conserved, apart from viscous coupling with the boundary (neglecting the small numerical effects) in our computations.

The change in total axial momentum during relaxation events in our two-fluid computations results from viscous and gyroviscous coupling to the boundary, and axial momentum is transported radially inward through the large Maxwell stress, as can be seen in Fig. 14 and Fig. 15. These figures show the axial momentum flux [terms in Eq. (11)] as a function of radius in case B and case C, respectively. Here, a positive term implies inward radial transport of momentum, while a negative term implies outward radial transport. In case B, viscous coupling to the boundary is responsible for nearly all of the axial momentum injected during relaxation, with additional small contributions from numerical effects. A thin boundary layer exists near  $r/a \lesssim 1$  in our computation with ion gyroviscosity, as the viscous and gyroviscous stresses compete with each other near the edge, but total axial momentum still increases during relaxation. The Maxwell stress peaks near  $r/a \approx 0.7$  and transports axial momentum further inward. In both computations the Reynolds stress generally opposes the Maxwell stress across the profile, but the magnetic relaxation is dominant, and the total axial momentum flux follows the Maxwell stress. Similar behavior is observed for the angular momentum flux.

Note that the flux of axial momentum is inward in the core region,  $r/a \lesssim 0.3$ , during the subsequent relaxation events shown here. The axial momentum is essentially the same as the parallel momentum in the core, where the

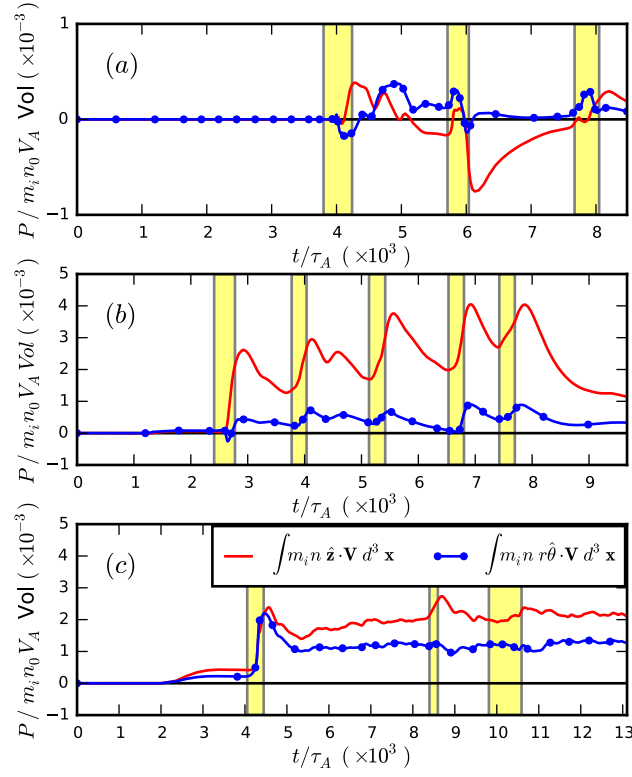


FIG. 13. Evolution of total axial and angular momenta for (a) case A: single-fluid MHD ( $\Lambda_e = 0$ ,  $\Lambda_i = 0$ ), (b) case B: two-fluid no gyroviscosity ( $\Lambda_e = 1$ ,  $\Lambda_i = 0$ ), (c) case C: two-fluid with gyroviscosity ( $\Lambda_e = 1$ ,  $\Lambda_i = 1$ ). Note axes differ.

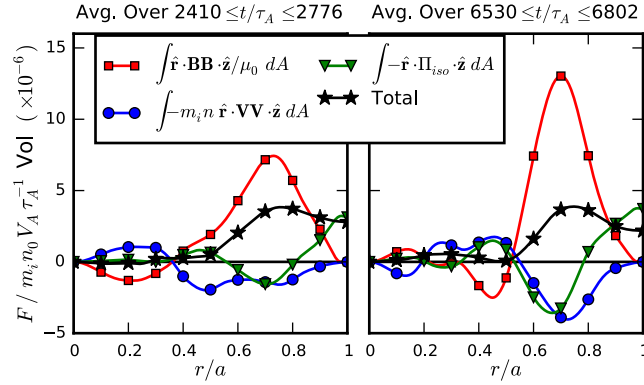


FIG. 14. Axial momentum flux averaged over two relaxation events in case B ( $\Lambda_e = 1$ ,  $\Lambda_i = 0$ ).

magnetic field is nearly axial. The increase in core plasma flow parallel to the magnetic field during the subsequent events in our computations is directly related to the inward radial transport of axial momentum via the Maxwell stress in these events.

The equilibrium pinch flow, neglected in Eq. (10), acts as an anomalous momentum sink, and it becomes slightly more significant during later events when momentum has been injected into the system. In the initial relaxation event in both two-fluid computations approximately 10% of the axial momentum that is transported radially inward by the Maxwell stress across  $r/a = 0.7$  is dissipated by this term. In the fourth relaxation event in our case B computation, this anomalous diffusion removes roughly 17% of the axial momentum transported by the Maxwell stress across  $r/a = 0.7$ , and it dissipates roughly 22.5% of the axial momentum transported across  $r/a = 0.7$  by the Maxwell stress in the second relaxation event of our case C computation. However, as mentioned previously, the equilibrium pinch flow scales as  $\sim 1/S$ , and this term is expected to be much less significant at more realistic parameters.

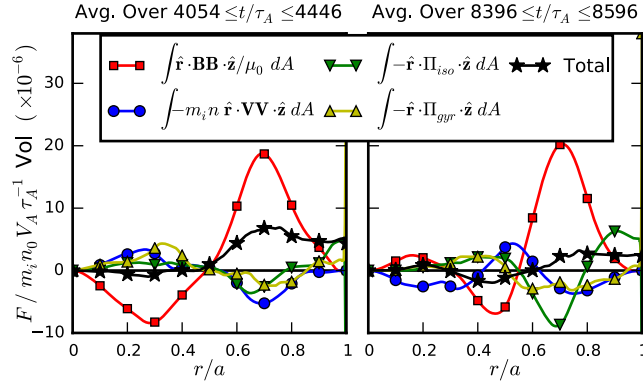


FIG. 15. Axial momentum flux averaged over two relaxation events in case C ( $\Lambda_e = 1$ ,  $\Lambda_i = 1$ ).

#### IV. CONCLUSIONS

Our single- and two-fluid computations display multiple discrete relaxation events during the self-consistently modeled nonlinear evolution, and macroscopic features, such as rapid drops in field reversal and magnetic fluctuation activity, are qualitatively consistent with experimental observations. In all relaxation events, the parallel current density profile is flattened through the action of fluctuation-induced dynamo electric fields. Two-fluid computations show significant contributions from the two-fluid Hall dynamo in addition to the standard single-fluid MHD dynamo. However, the sum of the MHD and Hall dynamos,  $-\langle \tilde{\mathbf{v}}_e \times \tilde{\mathbf{B}} \rangle$ , in our two-fluid computations appears similar to the MHD dynamo,  $-\langle \tilde{\mathbf{V}} \times \tilde{\mathbf{B}} \rangle$ , in our single-fluid computations. We infer that the energetically accessible relaxed states (quantified by  $F$ ) are sufficiently similar in the different models that the net dynamo effects that relax the dominant magnetic energy profiles are similar. Nevertheless, the decoupling of electron and ion dynamics allowed by the two-fluid effects leads to significantly different effects on the subdominant kinetic energy evolution.

The initial relaxation event in each simulation disrupts a QSH state, and in our two-fluid computations both the MHD and the Hall dynamo act to flatten the parallel current density profile. The corresponding Lorentz force density generates plasma flow in a direction opposite to the change in parallel current density, in agreement with the previous results of Ref. 7, but in contradiction to experimental observations. Subsequent relaxation events occur from multi-helicity conditions and are believed to be more representative of typical relaxation events in conventional RFP experiments. When the Hall dynamo opposes the MHD dynamo, the Lorentz force density generates core plasma flow in the direction of the change in parallel current density, in qualitative agreement with experimental observations. Whether events that terminate QSH states in experiments follow the behavior of the first events in our simulations can be tested by isolating the relevant data.

Dynamo competition in subsequent events is attributed to increased contributions from additional modes and a decreased contribution from the core-resonant  $m = 1, n = 6$  mode. We note that dynamo competition is observed more consistently in our computation with ion gyroviscosity, while in our computation without ion gyroviscosity, it is only observed during a relaxation event when the energy in the dominant  $m = 1, n = 6$  mode is smaller than it is during other events. We speculate that gyroviscous stabilization of the core-resonant  $m = 1, n = 6$  mode may aid in reducing that mode's contribution to core Hall dynamo, possibly altering the net Hall dynamo effect.

The variability of competition vs. cooperation between the two dynamo effects during relaxation events needs further study. Experimental measurements rely on ensemble averages of many similar relaxation events, and this averaging precludes a direct comparison to a single experimental event. In principle, it is possible to average over many relaxation events in two-fluid computations, but this is not done here owing to the small sample sizes. As longer two-fluid simulations become more practical, more informative statistical analyses can be applied.

Changes in axial and angular plasma momentum occur during our two-fluid computations and are associated with the discrete current relaxation events. We identify the cause as viscous and gyroviscous coupling to the boundary, and the inward radial momentum transport occurs through the fluctuation-induced Maxwell stress. We do not expect the viscous coupling to be representative of net momentum injection in the experiment. Investigation of the relevant physical effects that are active near the wall of the experiment awaits future modeling developments.

## ACKNOWLEDGMENTS

The authors acknowledge Prof. John Sarff, Joseph Triana, and other members of the MST experimental team for helpful discussions of relaxation activity in MST. This work was supported by NSF grant PHY-0821899, and by the U.S. Department of Energy grant DE-FG02-06ER54850. This research used resources of the National Energy Research Scientific Computing Center, a DOE Office of Science User Facility supported by the Office of Science of the U.S. Department of Energy under Contract No. DE-AC02-05CH11231.

- <sup>1</sup>H. Bodin and A. Newton, *Nuclear fusion* **20**, 1255 (1980).
- <sup>2</sup>H. P. Furth, J. Killeen, and M. N. Rosenbluth, *Physics of Fluids* (1958-1988) **6**, 459 (1963).
- <sup>3</sup>S. Ortolani and D. D. Schnack, *Magnetohydrodynamics of plasma relaxation*, Vol. 156 (World Scientific, 1993).
- <sup>4</sup>R. Dexter, D. Kerst, T. Lovell, S. Prager, and J. Sprott, *Fusion Science and Technology* **19**, 131 (1991).
- <sup>5</sup>A. Hansen, A. Almagri, D. Craig, D. Den Hartog, C. Hegna, S. Prager, and J. Sarff, *Physical Review Letters* **85**, 3408 (2000).
- <sup>6</sup>A. Kuritsyn, G. Fiksel, A. Almagri, D. Brower, W. Ding, M. Miller, V. Mirnov, S. Prager, and J. Sarff, *Physics of Plasmas* (1994-present) **16**, 055903 (2009).
- <sup>7</sup>J. King, C. Sovinec, and V. Mirnov, *Physics of Plasmas* (1994-present) **19**, 055905 (2012).
- <sup>8</sup>H. K. Moffatt, *Field Generation in Electrically Conducting Fluids* (Cambridge University Press, Cambridge, London, New York, Melbourne, 1978).
- <sup>9</sup>E. Caramana, R. Nebel, and D. Schnack, *Physics of Fluids* (1958-1988) **26**, 1305 (1983).
- <sup>10</sup>H. Strauss, *Physics of Fluids* (1958-1988) **28**, 2786 (1985).
- <sup>11</sup>D. Schnack, E. Caramana, and R. Nebel, *Physics of Fluids* (1958-1988) **28**, 321 (1985).
- <sup>12</sup>E. Hameiri and A. Bhattacharjee, *Physics of Fluids* (1958-1988) **30**, 1743 (1987).
- <sup>13</sup>K. Kusano and T. Sato, *Nuclear fusion* **27**, 821 (1987).
- <sup>14</sup>J. Holmes, B. Carreras, P. Diamond, and V. Lynch, *Physics of Fluids* **31**, 1166 (1988).
- <sup>15</sup>Y. Ho and G. Craddock, *Physics of Fluids B: Plasma Physics* (1989-1993) **3**, 721 (1991).
- <sup>16</sup>H. Ji, A. Almagri, S. Prager, and J. Sarff, *Physical Review Letters* **73**, 668 (1994).
- <sup>17</sup>D. Den Hartog, J. Chapman, D. Craig, G. Fiksel, P. Fontana, S. Prager, and J. Sarff, *Physics of Plasmas* (1994-present) **6**, 1813 (1999).
- <sup>18</sup>P. Fontana, D. Den Hartog, G. Fiksel, and S. Prager, *Physical Review Letters* **85**, 566 (2000).
- <sup>19</sup>R. Nebel, in *Proceedings of the Physics of Alternative Magnetic Confinement Schemes*, Vol. 1, edited by S. Ortolani and E. Sindoni (Editrice Compositori, Bologna (Italy), 1991) pp. 611–630.
- <sup>20</sup>J. King, C. Sovinec, and V. Mirnov, *Physics of Plasmas* (1994-present) **18**, 042303 (2011).
- <sup>21</sup>A. Schluter and L. Biermann, *Z. Naturforsch* **5** (1950).
- <sup>22</sup>C. Sovinec, J. King, N. Team, *et al.*, *Journal of Computational Physics* **229**, 5803 (2010).
- <sup>23</sup>J. Drake and Y. Lee, *Physics of Fluids* (1958-1988) **20**, 1341 (1977).
- <sup>24</sup>D. Biskamp, E. Schwarz, and J. F. Drake, *Physics of Plasmas* **4**, 1002 (1997).
- <sup>25</sup>W. Shen and S. Prager, *Physics of Fluids B: Plasma Physics* (1989-1993) **5**, 1931 (1993).
- <sup>26</sup>W. Ding, D. Brower, D. Craig, B. Deng, G. Fiksel, V. Mirnov, S. Prager, J. Sarff, and V. Svidzinski, *Physical Review Letters* **93**, 045002 (2004).
- <sup>27</sup>W. Ding, D. Brower, B. Deng, A. Almagri, D. Craig, G. Fiksel, V. Mirnov, S. Prager, J. Sarff, and V. Svidzinski, *Physics of Plasmas* (1994-present) **13**, 112306 (2006).
- <sup>28</sup>J. Triana, A. Almagri, K. McCollam, J. Sarff, and C. Sovinec, *Bulletin of the American Physical Society* (2016).
- <sup>29</sup>C. Sovinec, A. Glasser, T. Gianakon, D. Barnes, R. Nebel, S. Kruger, D. Schnack, S. Plimpton, A. Tarditi, M. Chu, *et al.*, *Journal of Computational Physics* **195**, 355 (2004).
- <sup>30</sup>J. Sauppe and C. Sovinec, *Physics of Plasmas* (1994-present) **23**, 032303 (2016).
- <sup>31</sup>S. Braginskii, *Reviews of plasma physics* **1**, 205 (1965).
- <sup>32</sup>D. Robinson, *Plasma Physics* **13**, 439 (1971).
- <sup>33</sup>H. Stephens, D. Den Hartog, C. Hegna, and J. Reusch, *Physics of Plasmas* (1994-present) **17**, 056115 (2010).
- <sup>34</sup>J. M. Finn, R. Nebel, and C. Bathke, *Physics of Fluids B: Plasma Physics* (1989-1993) **4**, 1262 (1992).
- <sup>35</sup>D. Escande, P. Martin, S. Ortolani, A. Buffa, P. Franz, L. Marrelli, E. Martines, G. Spizzo, S. Cappello, A. Murari, *et al.*, *Physical Review Letters* **85**, 1662 (2000).
- <sup>36</sup>L. Zakharov and B. Rogers, *Physics of Fluids B: Plasma Physics* (1989-1993) **4**, 3285 (1992).
- <sup>37</sup>B. Rogers, R. Denton, J. Drake, and M. Shay, *Physical Review Letters* **87**, 195004 (2001).
- <sup>38</sup>C. Hegna, *Physics of Plasmas* (1994-present) **5**, 2257 (1998).
- <sup>39</sup>R. Numata, Z. Yoshida, and T. Hayashi, *Computer physics communications* **164**, 291 (2004).